Fabrication and Characterization of Patterned Single-Crystal Silicon Nanolines[§]

Bin Li,[*,†] **Min K. Kang,**[‡] **Kuan Lu,**[†] **Rui Huang,**[*,‡] **Paul S. Ho,**[*,†] **Richard A. Allen,**[§] **and Michael W. Cresswell**[§]

[†] *Microelectronics Research Center, University of Texas, Austin, TX 78758*

[‡] *Department of Aerospace Engineering and Engineering Mechanics, University of Texas, Austin, TX 78712*

[§] *Semiconductor Electronics Division, National Institute of Standards and Technology, Gaithersburg, MD 20899*

Table of Content Graphic:
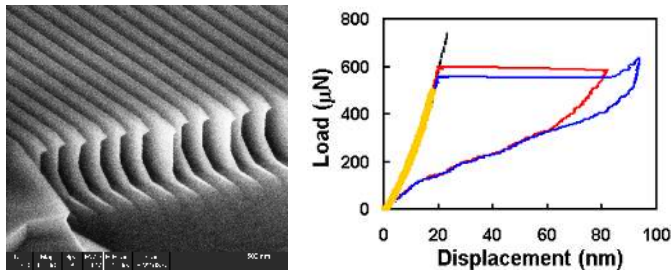
[*] To whom correspondence should be addressed. E-mail: libin@mail.utexas.edu (B.L.);

ruihuang@mail.utexas.edu (R.H.); paulho@mail.utexas.edu (P.S.H.).

ABSTRACT

This letter demonstrates a method to fabricate single-crystal Si nanolines, with rectangular cross sections and nearly atomically flat sidewalls. The high quality of these nanolines leads to superb mechanical properties, with the strain to fracture measured by nanoindentation tests exceeding 8.5% for lines of 74 nm width. A large displacement burst before fracture was observed, which is attributed to a buckling mechanism. Numerical simulations show that the critical load for buckling depends on the friction at the contact surface.

As the scaling of device dimensions continues, fabrication of nanoscale structures and characterization of their physical properties pose significant challenges for future development of ultra large-scale integrated (ULSI) and gigascale integrated (GSI) circuits.[1-3] In particular, silicon-based nanostructures are essential building blocks for nanoelectronic devices and nano-electromechanical systems (NEMS),[4-7] and their mechanical properties play an important role in controlling the functionality and reliability of the devices. Previously, single-crystal silicon (Si) beams with widths from 200 nm to 800 nm were fabricated by field-enhanced anodization using an atomic force microscope (AFM), typically with trapezoidal cross sections due to the anisotropic wet etching process.[8-10] Mechanical characterization of these Si beams by AFM bending tests showed a strong size effect on bending strength, which is the maximum tensile stress in a bent specimen up to fracture, but no size effect on Young's modulus.[8] The reported bending strength was in the range of 11 GPa to 18 GPa, significantly higher than the average strengths for microscale Si beams[11] (4 GPa) and millimeter scale Si beams[8] (around 500 MPa). It appears that the strength of nanoscale single-crystal Si beams could soon achieve the theoretical fracture strength of Si, predicted to be 22 GPa under tension with a critical strain of 17%.[12] More recently, a chemical-synthesis-based bottom-up approach has been developed to grow high-quality single-crystal Si nanowires (SiNWs) with diameters ranging from 50 nm to 350 nm.[5-7, 13-15] Different from the top-down fabricated Si beams, these SiNWs typically have hexagonal cross sections enclosed by {112} faceted crystalline planes.[7] Both single and double clamped SiNWs were characterized by AFM bending tests.[13-15] Again, no size effect was found for the Young's modulus.[13] For SiNWs with diameters between 90 nm and 200 nm, Hoffmann et al. [15] reported an average strength around 12 GPa, while Tabib-Azar et al.[14] reported much lower strengths in the range of 210 MPa to 830 MPa for longer SiNWs (10 μm vs 2 μm), possibly due to process-induced defects and friction at the contact between the AFM tip and the SiNWs. No data have

been reported so far for the strength of SiNWs with diameters less than 90 nm. As another technique to fabricate SiNWs, the superlattice nanowire pattern transfer (SNAP) method[16,17] was demonstrated and capable of producing parallel arrays of SiNWs with widths and pitches down to 10 nm and 40 nm, respectively. However, the SNAP process requires reactive ion etching (RIE) steps for pattern transfer into Si, which can potentially introduce defects in SiNWs.[17] While reasonably good electronic properties have been demonstrated,[18] no mechanical characterization has been reported for SNAP-produced SiNWs.

In addition to the AFM bending tests, other methods for nanoscale mechanical characterization have been developed, such as mechanical resonance,[19,20] nano-tensile,[21-23] and nanoindentation tests.[24-30] In general, characterization of mechanical properties at the nanoscale level requires precise manipulation of nanoscale specimens and high-resolution force/displacement measurements. The resonance method is limited to the measurement of elastic properties only, and the AFM-based bending and tensile tests are often challenging due to the difficulty in sample preparation and calibration.[31] The nanoindentation technique has been well established for the measurement of elastic modulus, hardness, and fracture toughness of both bulk and thin film materials.[32,33] The precision in both force and displacement measurements together with easy sample preparation have led to recent applications of this technique for mechanical characterization of various nanomaterials including nanotubes,[24,27] nanowires,[25,30] nanobelts,[26] and nanoparticles.[29] However, interpretation of the nanoindentation result is nontrivial and often requires sophisticated modeling.[27,30,34,35]

In this study, we demonstrate a top-down fabrication process combining electron-beam lithography (EBL) and anisotropic wet etching to obtain single-crystal, parallel Si nanolines (SiNLs) on a Si (110) wafer. An AFM-based nanoindentation technique along with numerical simulations by a finite element method (FEM) is employed to characterize the mechanical

properties of the SiNLs, yielding the elastic modulus, the strain to fracture of the SiNLs, and the

friction coefficient at the contact with the indenter tip. This demonstrates a novel

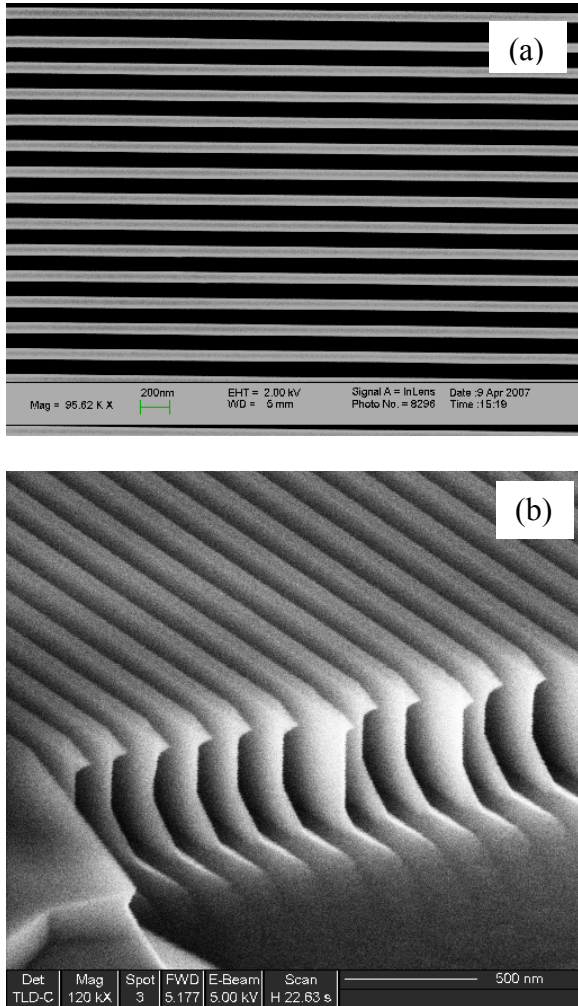nanomechanical testing method of patterned nanostructures.

Figure 1. SEM images of the parallel silicon nanolines, with 74 nm line width and 510 nm height. The line pitch is 180 nm. (a) Plane view; (b) Cross-sectional view with 60° tilt angle. A small trench pattern is specially designed at one end of the line to facilitate the cross-sectional SEM imaging, showing the sharp edges due to the anisotropic etching.

The fabrication of the SiNLs shown in Figure 1 was inspired by a process featured i-line

lithography with a 365 nm light source and anisotropic wet etching, which was used for

fabrication of critical-dimension reference standards.[36,37] The anisotropic wet etching process has

proven capable of producing nearly atomically flat sidewalls without ion-bombardment or

plasma induced defects.[36,37] To reduce the line dimensions, we used EBL to obtain line widths less than 100 nm. EBL is capable of producing patterns with feature dimension as small as 20 nm.[38] Unlike conventional EBL techniques that require RIE or lift-off processes for pattern transfer,[38] the present fabrication process effectively combines the high resolution of EBL with high quality pattern transfer by anisotropic wet etching. Comparing to similar structures produced by pattern transfer with RIE steps (Supporting Information), these SiNLs have much smoother sidewalls with almost perfectly rectangular cross sections and a highly uniform line width. With well-defined crystalline and geometric features, these SiNLs have potential applications for nanograting-based sensors[39] and interconnects,[5] and they are also well-suited for quantitative studies of nanomechanics (e.g., fracture and friction).

The fabrication began with a thin chromium coating deposited on a Si (110) wafer which was covered with an oxide layer by chemical vapor deposition. After the chromium coating, a positive photoresist was spun on the wafer and then imaged using an electron-beam exposure system. The pattern was first transferred from the resist layer to the chromium lines by plasma etching. The chromium layer is then used as a hard mask for patterning the oxide layer by a reactive ion etching (RIE) process.[40] Subsequently, the residual resist was removed and tetra-methyl-ammonium hydroxide (TMAH) was used for anisotropic etching of the Si along {111} crystalline planes. The oxide layer serves as an etching mask for pattern transfer to silicon. When the patterned openings were aligned with one of the <112> directions in the (110) plane, vertical and nearly atomically flat sidewalls were formed with the {111} orientation. Finally, the chromium and oxide hard masks were removed by chromium etchant and buffered oxide etchant, respectively. Figure 1 shows the scanning electron microscope (SEM) images of the parallel patterned SiNLs with 74 nm line width. The height of these SiNLs is about 510 nm, corresponding to an aspect ratio of 6.9 for the rectangular cross section. Using the same

approach, we have successfully fabricated SiNLs with line widths ranging from 40 nm to 500 nm, and a line width as small as 20 nm is achievable. The height of the SiNLs can be controlled by TMAH etching time within the range of 100 nm to 2000 nm, and the length is defined by the exposed electron-beam patterning area which was 50 μm for the present study. The high crystal quality and well-defined geometry, along with the smooth sidewalls and the highly uniform line width, make these SiNLs well suited for accurate experimental measurements as well as numerical modeling.
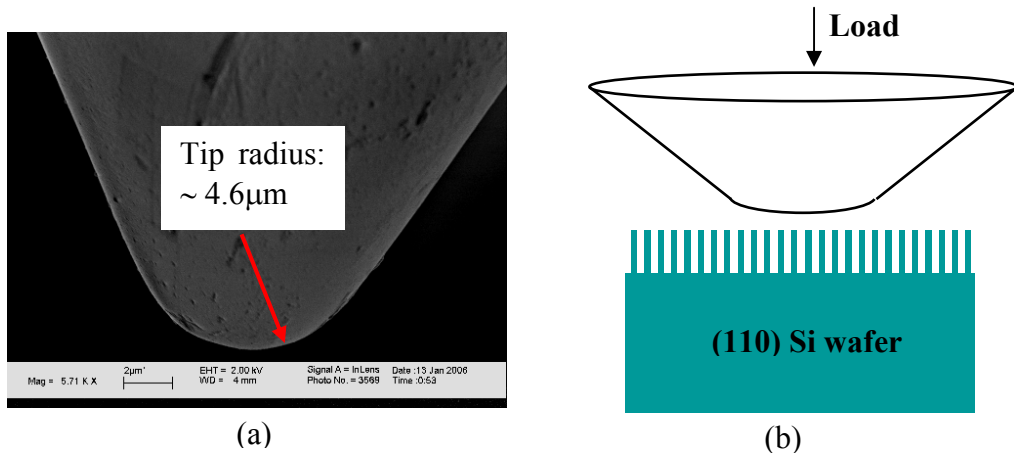

(a)   (b)

Figure 2. (a) An SEM image of the conical-shaped indenter with the tip radius around 4.6 μm; (b) Schematic illustration of the nanoindentation experiment on silicon nanolines.

In the measurements an AFM based nanoindentation system (Tribescope by Hysitron, Inc.)[1] was used to characterize the mechanical properties of the SiNLs. A conical shaped indenter with the tip radius around 4.6 μm (as determined from the SEM image in Figure 2a) was used to probe the parallel SiNLs, as schematically illustrated in Figure 2b. During each indentation test the indenter was placed directly above a 50 μm by 50 μm array of parallel nanolines. Subsequently,

---

[1] Certain commercial equipment, instruments, or materials are identified in this document in order to specify measurement procedures adequately. Such identification does not imply recommendation or endorsement by the National Institute of Standards and Technology, nor does it imply that the materials or equipment identified are necessarily the best available for the purpose.

the indenter was brought into contact with the SiNLs, and a transducer was used to monitor and record the indentation loading and unloading process with force and displacement measured simultaneously.[41,42] In the indentation tests, the peak loads ranged from 500 μN to 1000 μN, with a force resolution of ~0.2 μN and displacement resolution of ~0.2 nm.

Figure 3 shows three force-displacement curves obtained from the nanoindentation tests on the 74 nm SiNLs. For the first test (yellow in Figure 3), a small indentation load of 500 μN was applied and subsequently unloaded, which shows an elastic response with coinciding curves for loading and unloading. With the indentation load increased beyond 550 μN, a large displacement burst without load increase was observed, as shown in Figure 3 for the second and third tests (red and blue). This indicates the occurrence of an instability of the SiNLs under indentation. Similar displacement bursts were observed in nanoindentation experiments of metal films, which were attributed to a dislocation mechanism as an intrinsic material instability.[34] Here, however, the magnitude of the displacement burst is much larger (over 60 nm in comparison with a few nanometers for the metal films). As noted in a previous study,[9] plastic deformation of nanoscale single-crystal Si beams was observed only at elevated temperatures (>373° K); thus, the dislocation mechanism is not expected to operate at room temperature. Furthermore, it was found that after the displacement burst, the displacement was fully recovered upon unloading of the indenter. This suggests that the material remains elastic before and after the displacement burst, where the instability is most likely due to buckling of the SiNLs. Buckling as an elastic instability has been observed in other nanostructures.[21,27,43,44] In particular, the observation of full displacement recovery of the parallel SiNLs after buckling is similar to the reported supercompressible behavior of foam-like carbon nanotube (CNT) films.[44] The latter was

attributed to a cooperative buckling mechanism of the vertically aligned carbon nanotubes (VACNTs). The buckling mechanism of the SiNLs will be discussed later in this paper.
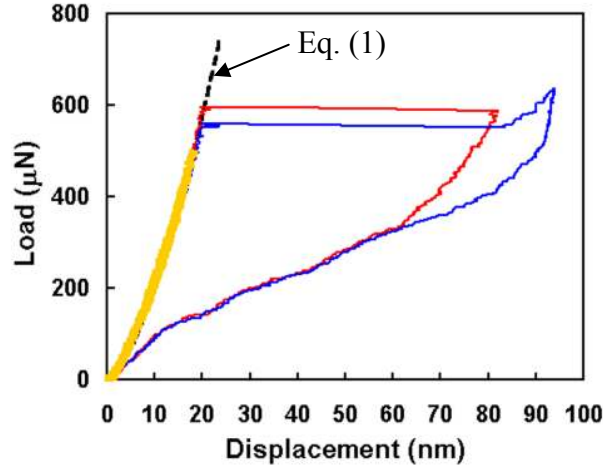

Figure 3. Load vs. displacement curves of a set of nanoindentation tests of parallel SiNLs with 74 nm line width and 510 nm height. For the three indentation tests (yellow, red and blue), no residual deformation was observed after withdrawal of the indenter. The dark line represents the theoretically predicted elastic response by Eq. (1) using an effective modulus $E^* = 72$ GPa.

To understand the nanoindentation results, we start with the well-known Hertz theory of contact mechanics for a spherical indenter onto a planar surface,[32] which predicts a force-displacement relationship as follows:

$$P = \frac{4}{3} E^* h^{3/2} R^{1/2} \tag{1}$$

where P is the indentation load (force), h is the indentation depth (displacement), R is the radius of the spherical indenter, and E^* is an effective modulus. For indentation on a planar surface, the effective modulus is: $\frac{1}{E^*} = \frac{1-v_1^2}{E_1} + \frac{1-v_2^2}{E_2}$, where E is Young's modulus and v is Poisson's ratio, with the subscripts 1 and 2 referring to the indenter and the indented materials, respectively. For the present study, however, the Si surface was patterned with parallel SiNLs. It is found that the initial portion of the load-displacement curves in Figure 3 can be well fitted by Eq. (1) with an effective modulus, $E^* = 72$ GPa. This value is significantly lower than the effective modulus

calculated with the elastic moduli of Si and diamond for indentation on a planar surface. As would be expected, the material removal due to nanoscale patterning effectively reduces the stiffness of the Si surface under indentation. Consequently, the Hertz theory cannot be directly applied for the indentation tests on SiNLs. Since the tip radius of the indenter (~4.6 μm) is much larger than the pitch of the SiNLs (180 nm), we did not have the lateral resolution in the indentation system to identify the exact location of the indenter tip relative to the individual SiNLs, which could vary from a trench center to a line center of the parallel pattern. Nevertheless, it is noted from Figure 3 that the initial elastic response (before the displacement burst) of the SiNLs was reproducible, thus insensitive to the relative location of the indenter tip, which is similar to the response of a film-like material.

The deviation from the initial elastic response occurred with a displacement burst at a critical load in the range of 480 μN to700 μN (see Figure 3 and Figure 6a). This has been attributed to a buckling instability of the SiNLs and is simulated by using a three-dimensional (3D) finite element model as shown in Figure 4. A spherical indenter on six parallel lines is modeled using the commercial FEM package ABAQUS,[45] with the tip of the indenter located at the trench center. It was found that adding more lines does not change the simulation results for the initial elastic response and the critical load. Since the modulus of the diamond tip (1140 GPa) is much higher than the modulus of Si, the indenter is modeled as a rigid body. The Si lines are supported at the bottom by a rigid substrate as an approximation for the un-etched part of the Si wafer. It was found that modeling with an elastic substrate gives a slightly lower critical load but significantly increases the computational time. The contact between the tip and the lines was initially assumed to be frictionless. The numerical simulation used the static Riks method.[46]

Figure 4a shows the force-displacement curve obtained from the simulation, where the dashed curve is identical to that in Figure 3 predicted by Eq. (1) with $E^* = 72$ GPa. A comparison
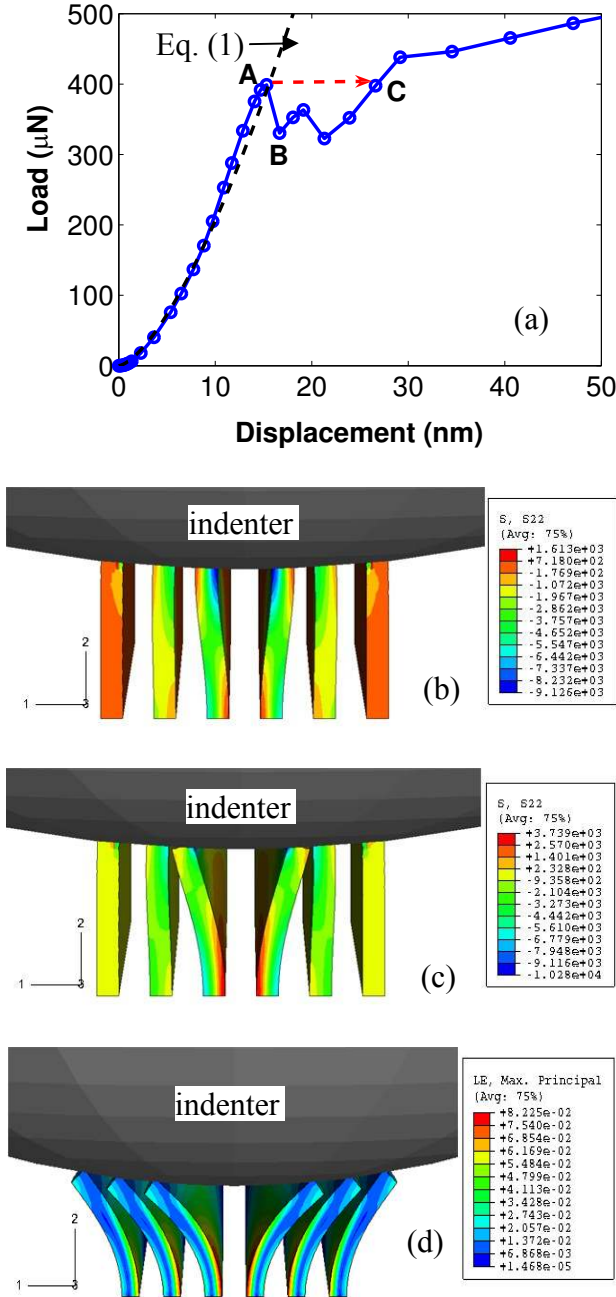
Figure 4. Finite element modeling of the silicon nanolines under indentation. The tip of the indenter is located on top of the trench center of the 74 nm silicon nanolines. (a) plots the simulated load-displacement curve, while the dashed line represents the theoretically predicted elastic response by Eq. (1) using an effective modulus $E^* = 72$ GPa. At the critical load (marked as A), the simulation predicts a drop in force from A to B due to the transition of the buckling mode. Under a load-control experiment, the simulation predicts a displacement burst from A to C. (b) and (c) show the deformation and stress distribution before and after the mode transition at the critical load, corresponding to A and B marked in (a), respectively. (d) shows the deformation of the nanolines from a simulation with 90 nm indentation displacement, for an estimation of the strain to fracture.

11

between Figure 3 and Figure 4a shows that the initial elastic response from the 3D model agrees well with the experimental data. The elastic properties of the SiNLs used in this simulation were: Young's modulus $E = 140$ GPa and Poisson's ratio $v = 0.27$. This modulus is lower than that for bulk Si in the <110> directions (169 GPa). As previous studies of Si beams[8] and SiNWs[13] showed no size effect in the elastic modulus of Si, the discrepancy is mainly attributed to the approximations in the numerical model that assumed a rigid indenter, a rigid substrate, and isotropic elastic properties.

At a critical load (marked as A in Figure 4a), the simulation predicts a drop of the indentation load under the displacement control. This is an indication of softening of the nanolines under the indentation, which would lead to a displacement burst during a load-control experiment. The critical load for the displacement burst can be determined from the first peak of the simulated curve. Figures 4 (b) and (c) show the simulated deformation of the nanolines immediately before and after the critical load, from which we see a transition of the buckling mode. Before the critical load, the center two lines are bent symmetrically into a half-wave mode with the top nearly perpendicular to the surface of the indenter. After the critical load, the lines are bent into a quarter-wave mode, which is structurally softer than the half-wave mode. Such a transition leads to the drop of the indentation load (from A to B) under the displacement control, or equivalently, a displacement burst (from A to C) under the load control. The second peak in the simulated load-displacement curve is the result of a similar transition for the next two lines, which would not be observed in the load-control experiments. Figure 4 (b) shows that the SiNLs are deformed by both compression and bending even before the displacement burst, while the stress contour shows largely compressive stresses in the SiNLs except for localized tensile stresses due to bending. It is noted that the magnitude of the displacement burst predicted by the static simulation is much smaller than that observed in experiments. This may be addressed by using a

more accurate model that take into account the dynamic postbuckling behavior. Nevertheless, the present model is sufficient for the simulation of the initial elastic response and the prediction of the critical load. It may be pointed out that the transition of buckling mode is a rather unique behavior, owing to the high aspect ratio and nearly perfect rectangular cross sections of the nanolines.

It is found that the critical load as predicted by the numerical model depends on the relative location of the indenter tip on top of the nanolines and the friction at the contact between the Si lines and the indenter. The relative location of the indenter was varied from the trench center to the line center of one side in the simulations. It was found that the relative location has insignificant influence on the initial elastic response, confirming the film-like behavior under a relatively large indenter. On the other hand, the critical load increases significantly when the indenter is located on the line center. This may be responsible for the scattering of the critical loads from the indentation tests as we did not have the lateral resolution of the indentation system to identify the exact location of the indenter. The friction at the nanoscale contact is of fundamental interest. Here, by using a simple Coulomb friction model, we found that the critical load increases as the friction constant at the contact increases. On the other hand, the frictional contact property does not influence the initial elastic response under indentation. Figure 5 plots the predicted critical load as a function of the friction constant, with the indenter located at the trench center and the line center as the lower and upper bounds, respectively. Without friction, the Si lines slide freely along the surface of the indenter. This leads to a relatively low critical load of about 400 μN. The critical load thus offers an indirect measure of the friction at the nanoscale contact. Taking 480 μN as the lower bound for the critical load (see Figure 6a), the friction coefficient at the contact is estimated to be about 0.01. This value is about one order of magnitude lower than those obtained from a tribological test using a spherical diamond tip (tip

radius 20 μm) on single-crystal Si (100) wafers.[47] The present study suggests that the effect of contact friction may also be important in other nanomechanical tests such as the AFM bending tests of nanowires and nanobelts.
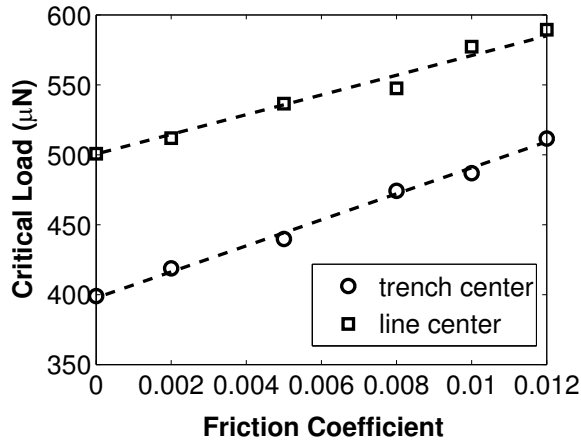

Figure 5. The critical indentation load predicted by the finite element model, as a function of the friction coefficient between the indenter tip and the Si nanolines. The two lines are for the tip located at the trench center and the line center, respectively, as the lower and upper bounds for the critical load.

Additional indentation tests with the SiNLs, which are shown in Figure 6a, showed irrecoverable residual deformation after unloading of the indenter. Here the maximum indentation displacement for each test is greater than 150 nm, while in Fig. 3 the maximum displacement is less than 100 nm. The larger indentation displacement implies more significant bending of the SiNLs after the buckling instability, which in turn induces higher tensile stresses that eventually fracture the SiNLs. Figure 6b shows the SEM image of the SiNLs with irrecoverable deformation due to fracture. The debris of the fractured SiNLs are of isosceles triangular shape in the (111) crystalline plane parallel to the SiNLs, with two sides in <110> directions and the base side in the <112> direction of the SiNLs. As shown by the schematic drawing in Figure 6c, the two side planes of the triangular debris were formed as a result of fracture along the $(1\bar{1}\bar{1})$ and $(\bar{1}1\bar{1})$ crystalline planes, indicating a primary cleavage mechanism

of the close packed {111} planes along the <110> directions.[33] The triangular shape is also a reflection of the buckling-induced tensile stress distribution in the SiNLs, which intensifies along the bending ridges of the nanolines under the indenter. To estimate the critical strain to fracture, a finite element simulation was conducted up to 90 nm indentation depth as shown in Figure 4d, from which we obtain a maximum principal strain of 8.5%. Although the present model is not accurate for the postbuckling analysis, the strain as a geometric measure serves as a reasonable estimation for the deformation of the SiNLs. Since the SiNLs did not fracture up to a 90 nm indentation depth as shown in Figure 3, the strain to fracture for the SiNLs is estimated to be above 8.5%. This strain is comparable to those reported by Hoffmann et al.[15] for SiNWs, but still significantly lower than the theoretical critical strain (17%) for Si[12] under tension in the <111> direction. The high crystalline quality and surface smoothness of the nanolines are critical for the observation of cleavage fracture of Si at the nanoscale, as the fracture process is highly sensitive to the surface defects.

In summary, this study demonstrates for the first time the feasibility of a method to fabricate single-crystal Si nanolines by combining electron-beam lithography with an anisotropic wet etching process. The Si nanolines have nearly atomically flat sidewalls with almost perfectly rectangular cross sections and highly uniform linewidth. Using an atomic force microscope (AFM) based nanoindentation system, the elastic, fracture, and frictional properties of the Si nanolines were characterized. A buckling instability was observed at a critical load, with fully recoverable deformation after a displacement burst. A finite element model was developed to simulate the elastic response and to predict the critical load. It was found that the critical load for buckling instability is sensitive to the friction coefficient of the contact. For experiments with larger indentation displacements, irrecoverable indentation displacements were observed due to fracture of Si nanolines, with the strain to failure estimated to be above 8.5%. The fracture debris

are of isosceles triangular shape along specific crystalline orientations, indicating a cleavage fracture mechanism under the effect of buckling induced stress distribution. This study demonstrates a valuable approach for nanoscale mechanical characterization using well-defined nanoline structures and the nanoindentation method.
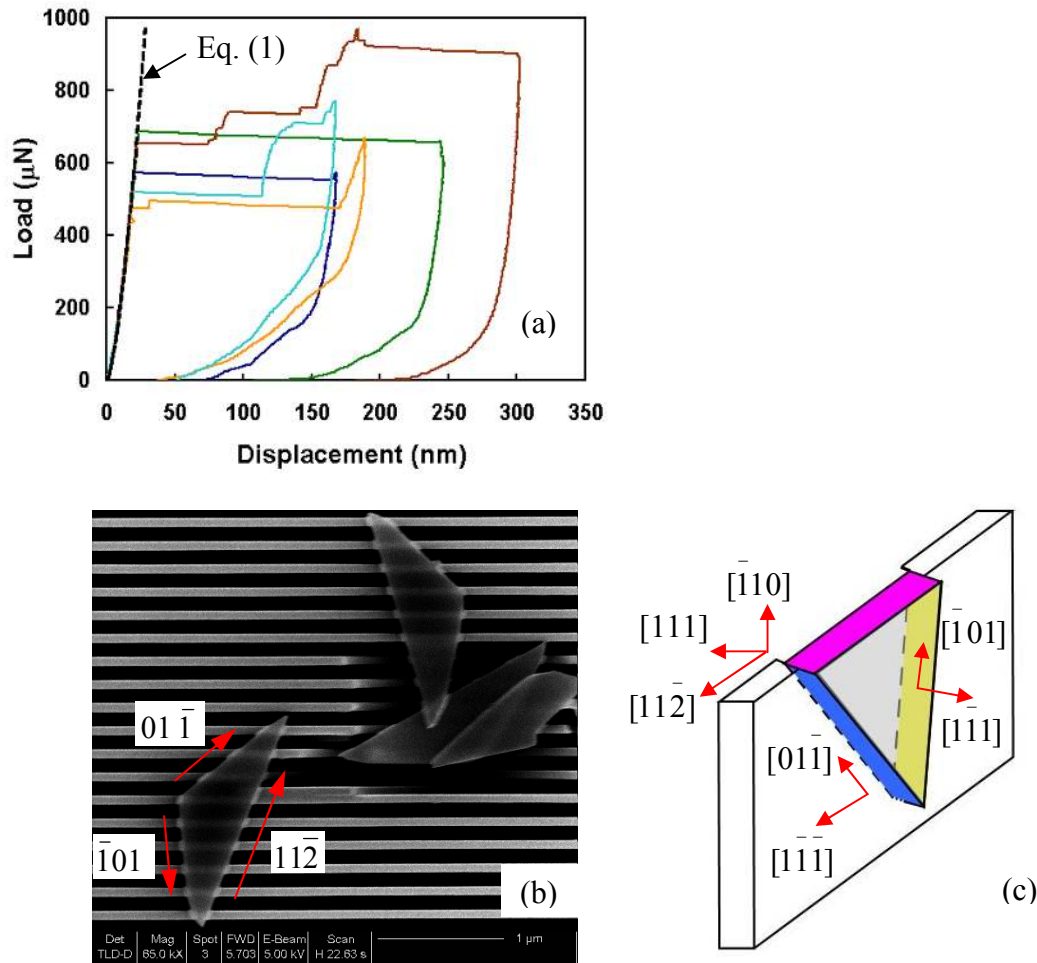

Figure 6. Results of nanoindentation tests on the 74 nm Si nanolines with irrecoverable displacements. (a) Load vs. displacement curves from 5 indentation tests. Fracture of the SiNLs led to large residue displacement after unloading of the indenter. The dark line denotes the elastic response of the nanolines without buckling as predicted by Eq. (1) with the effective modulus, E^* = 72 GPa; (b) An SEM image of the fractured nanolines after one indentation test. The fracture debris are of isosceles triangular shape in the (111) crystalline plane, indicating a cleavage fracture mechanism; (c) Schematic illustration of the crystalline orientations for the Si nanolines and the cleavage planes in the formation of the triangular fracture debris. The two side planes of the debris were formed as a result of fracture along the ($1\bar{1}\bar{1}$) (blue shaded) and ($11\bar{1}$) (yellow shaded) crystalline planes.

Supporting Information Available: SEM images of silicon nanolines produced by anisotropic wet etching and those by reactive ion etching, FEM simulation showing confined buckle deformation of the SiNLs after the displacement burst. This material is available free of charge via the Internet at http://pubs.acs.org.

REFERENCES:

(1) Wang, C.; Jones, R. L.; Lin, E. K.; Wu, W., Leu, J. *Appl. Phys. Lett.* **2007**, 90, 193122.

(2) Knight, S.; Dixson, R. G.; Jones, R. L.; Lin, E. K.; Orji, N.G.; Silver, R.; Villarrubia, J. S.; Vladár, A. E.; Wu, W. *Comptes Rendus Physique*, **2006**, 7, 931.

(3) Dixson, R.G.; Allen, R. A.; Guthrie, W. F.; Cresswell, M. W. *J. Vac. Sci. Technol. B* **2005**, 23, 3028.

(4) Lieber, C. M.; Wang, Z. L. *MRS Bulletin* **2007**, 32, 99.

(5) Saif Islam, M.; Sharma, S.; Kamins, T. I.; Williams, R. S. *Appl. Phys. A.* **2005**, 80, 1133.

(6) He, R.; Yang, P. *Nature Nanotechnology* **2006**, 1, 42.

(7) Feng, X. L.; He, R.; Yang, P.; Roukes, M. L. *Nano Lett.* **2007**, 7, 1953.

(8) Namazu, T.; Isono, Y.; Tanaka, T. *J. Microelectromechanical Systems* **2000**, 9, 450.

(9) Namazu, T.; Isono, Y.; Tanaka, T. *J. Microelectromechanical Systems* **2002**, 11, 125.

(10) Li, X.; Bhushan, B.; Takashima, K.; Baek, C.-W.; Kim, Y.-K. *Ultramicroscopy* **2003**, 97, 481.

(11) Johansson, S.; Schweitz, J.-A.; Tenerz, L.; Tiren, J. *J. Appl. Phy.* **1988**, 63, 4799.

(12) Roundy, D.; Cohen, M. L. *Phys. Rev.* B **2001**, 64, 212103.

(13) San Paulo, A.; Bokor, J.; Howe, R. T.; He, R.; Yang, P.; Gao, D.; Carraro, C.; Maboudian, R. *Appl. Phys. Lett.* **2005**, 87, 053111.

(14) Tabib-Azar, M.; Nassirou, M.; Wang, R.; Sharma, S.; Kamins, T. I.; Islam, M. S.; Williams, R. S. *Appl. Phys. Lett.* **2005**, 87, 113102.

(15) Hoffmann, S.; Utke, I.; Moser, B.; Michler, J.; Christiansen, S. H.; Schmidt, V.; Senz, S.; Werner, P.; G ösele, U.; Ballif, C. *Nano Lett.* **2006**, 6, 622.

(16)   Melosh, N. A.; Boukai, A.; Diana, F.; Gerardot, B.; Badolato, A.; Petroff, P. M.; Heath, J. R. *Science* **2003**, 300, 112.

(17)   Beckman, R. A.; Johnston-Halperin, E.; Melosh, N. A.; Luo, Y.; Green, J. E.; Heath, J. R. *J. Appl. Phys*. **2004**, 96, 5921.

(18)   Wang, D.; Sheriff, B. A.; Heath, J. R. Nano Letters 2006, 6, 1096.

(19)   Treacy, M. M. J.; Ebbesen, T. W.; Gibson, J. M. *Nature* **1996**, 381, 678.

(20)   Poncharal, P.; Wang, Z. L.; Ugarte, D.; de Heer, W. A. *Science* **1999**, 283, 1513.

(21)   Yu, M.-F.; Lourie, O.; Dyer, M. J.; Moloni, K.; Kelly, T. F.; Ruoff, R. S. *Science* **2000**, 287, 637.

(22)   Zhu, Y.; Espinosa, H. D. *Proc. Natl. Acad. Sci. USA* **2005**, 102, 14503.

(23)   Huang, J. Y.; Chen, S.; Ren, Z. F.; Wang, Z.; Kempa, K.; Naughton, M. J.; Chen, G.; Dresselhaus, M. S. *Phys. Rev. Lett.* **2007**, 98, 185501.

(24)   Yu, M.-F.; Kowalewski, T.; Ruoff, R. S. *Phys. Rev. Lett.* **2000**, 85, 1456.

(25)   Li, X.; Gao, H.; Murphy, C. J.; Caswell, K. K. *Nano Lett.* **2003**, 3, 1495.

(26)   Mao, S. X.; Zhao, M.; Wang, Z. L. *Appl. Phys. Lett.* **2003**, 83, 993.

(27)   Qi, H. J.; Teo, K. B. K.; Lau, K. K. S.; Boyce, M. C.; Milne, W. I.; Robertson, J.; Gleason, K. K. *J. Mech. Phys. Solids* **2003**, 51, 2213.

(28)   Uchic, M. D.; Dimiduk, D. M.; Florando, J. N.; Nix, W. D. *Science* **2004**, 305, 986.

(29)   Deneen, J.; Mook, W. M.; Minor, A.; Gerberich, W. W.; Carter, C. B. *J. Mater. Sci*. **2006**, 41, 4477.

(30)   Feng, G.; Nix, W. D.; Yoon, Y.; Lee, C. J. *J. Appl. Phys.* **2006**, 99, 074304.

(31)   Ding, W.; Guo, Z.; Ruoff, R. S. *J. Appl. Phys.* **2007**, 101, 034316.

(32)   Oliver, W. C.; Pharr, G. M. *J. Mater. Res.* **1992**, 7, 1564.

(33)   Cook, R. F. *J. Mat. Sci.* **2006**, 41, 841.

(34) Li, J.; Van Vliet, K. J.; Zhu, T.; Yip, S.; Suresh, S. *Nature* **2002**, 418, 307.

(35) Chen, X.; Ogasawara, N.; Zhao, M.; Chiba, N. *J. Mech. Phys. Solids* **2007**, 55, 1618.

(36) Cresswell, M. W.; Guthrie, W. F.; Dixson, R. G.; Murabito, C. E.; De Pinillos, J. V. M. *J. Res. Natl. Inst. Stand. Technol.* **2006**, 111, 187.

(37) Allen, R. A.; am Ende, B. A.; Cresswell, M. W.; Murabito, C. E.; Headley, T. J.; Guthrie, W. F.; Linholm, L. W.; Ellenwood, C. H.; Bogardus, E. H. *IEEE Trans. Semiconduct. Manufact.* **2003**, 16, 239.

(38) Vieu, C.; Carcenac, F.; Pepin, A.; Chen, Y.; Mejias, M.; Lebib, A.; Manin-Ferlazzo, L.; Couraud, L.; Launois, H. *Appl. Surf. Sci*. 2000, **164**, 111.

(39) Zhang, X. J.; Zappe, S.; Bernstein, R. W.; Sahin, O.; Chen, C.-C.; Fish, M.; Scott, M. P., Solgaard, O. *Sensors and Actuators* A **2004**, 114, 197.

(40) Smith, K. H.; Wasson, J. R.; Mangat, P. J. S.; Dauksher, W. J.; Resnick, D. J. *J. Vac. Sci. Technol. B*, **2001**, 19, 2906.

(41) User's Manual to Triboscope, Hysitron Inc., **1997**, Minneapolis, USA.

(42) Bhushan, B.; Kulkarni, A. V.; Bonin, W.; Wyrobek, J. T. *Phi. Mag. A*, **1996**, 74, 1117.

(43) Wong, E. W.; Sheehan, P. E.; Lieber, C. M. *Science* **1997**, 277, 1971.

(44) Cao, A.; Dickrell, P. L.; Sawyer, W. G.; Ghasemi-Neijhad, M. N.; Ajayan, P. M. *Science*, **2005**, 310, 1307.

(45) ABAQUS Documentation (Version 6.6), ABAQUS, Inc., **2006**, Providence, RI.

(46) Riks, E. *Int. J. Solids. Structures*, **1979**, 15, 529.

(47) Bhushan, B.; Li, X. *J. Mater. Res.*, **1997**, 12, 54.